

Geometric Shape Features Extraction Using a Steady State Partial Differential Equation System

T. Yamada^{a,*}

^a*Department of Mechanical Engineering and Science, Kyoto University, C3
Kyoto-Daigaku-Katsura, Nishikyo-Ku, Kyoto, 615-8504, Japan.*

Abstract

A unified method for extracting geometric shape features from binary image data using a steady state partial differential equation (PDE) system as a boundary value problem is presented in this paper. The PDE and functions are formulated to extract the thickness, orientation, and skeleton simultaneously. The main advantages of the proposed method is that the orientation is defined without derivatives and thickness computation is not imposed a topological constraint on the target shape. A one-dimensional analytical solution is provided to validate the proposed method. In addition, two and three-dimensional numerical examples are presented to confirm the usefulness of the proposed method.

Keywords: Partial differential equations; Geometric shape features; Shape analysis; Finite element method; Computer aided engineering

1. Introduction

The development of remarkable image analysis technology in recent years has helped solve many problems in various fields, such as materials science [1], mechanical engineering [2], biomechanics [3, 4], and medicine [5, 6]. For example, the skeleton can be extracted from computed tomography (CT) and magnetic resonance imaging (MRI) data, contributing to an understanding of

*Corresponding author

Email address: `takayuki@me.kyoto-u.ac.jp` (T. Yamada)

its structure. In particular, estimating local thickness is one significant measure for disease propagation. In reverse engineering of mechanical products [7], extracting geometrical features (e.g., curvature and edge information) from X-ray CT images is an important analytical technique when designing and developing new high performance systems in short time. When designing mechanical products, extraction of members that violating allowed minimal thickness in computer-aided design (CAD) models is an important design item. Therefore, feature extraction are used in a variety of computer vision, image processing, and digital engineering tasks.

This paper presents a unified method for extracting geometric features by using a partial differential equation (PDE). In the following section, related research on feature extraction and PDE-based image processing are briefly discussed. Second, the basic concept and overview of my proposed method are discussed by comparing related research with the proposed method. Next, a PDE for geometric shape feature extraction is formulated. The shape feature functions for thickness, orientation, and skeleton are formulated based on the proposed PDE. That is, these geometric features are represented as a function of the solution of PDE. In addition, a numerical algorithm for the proposed method based on finite element method (FEM) is presented. In Section 6, the validity of the proposed method is discussed based on a one-dimensional analytical solution. Finally, in order to confirm the validity and utility of the proposed method, several numerical examples are provided for two and three dimensional cases.

2. Related Works

Tensor scale is a measure of shape features that represents thickness, orientation, and anisotropy [8, 9]. The measure defines the parameters of the largest ellipse within the target domain at each pixel point. Although the measure in the proposed method represents several geometric features simultaneously, it incurs high computational cost because the Euclidean distance is computed for

each point.

Carne et al. [10] propose a PDE-based method for distance computation. The basic concept involves considering a fictitious heat diffusion equation with Dirichlet boundary conditions for a short time. Then, the distance is approximated using the fundamental solution of the fictitious temperature. Although the linear diffusion equation gives smooth solution and low computational cost, the heat effect reaches infinite distance even in a short time. Therefore, the method cannot be used to derive exact distance from a theoretical perspective.

Related research on feature extraction are briefly discussed as follows:

Thickness: One significant application of thickness extraction is in determining bone thickness [11, 12]. The local thickness defined in [5] is estimated based on a fuzzy distance transformation [13] in these methods. The process requires sampling depth at axial voxels, which are computed by skeletonization techniques[14, 15]. Another challenging application of measuring thickness is estimating the cortical thickness of the human brain from MRI data [6, 16]. These methods are classified as surface-based, voxel-based, and hybrid methods. In these methods, an image is separated into three domains: grey matter, white matter, and cerebrospinal fluid. As discussed in [16], the surface-based method [17] uses a generated mesh on one side surface. Next, the mesh is deformed to fit the pair surface under a topological constraint. In general, calculating advection requires high computational cost to ensure the consistent topology [18].

On the other hand, voxel-based methods are separated into morphological, line integral, diffeomorphic registration, and Laplacian-based methods. The morphological method [19] divides each voxel into inner and outer domains. The thickness is computed using a Euclidean distance transformation. In line integral based approaches [20, 21], every line integral centered at each point is computed and the minimum value is defined as the thickness. Diffeomorphic registration [22] also requires calculating surface deformation. Jones et al. [23] proposed the Laplacian-based approach. In this method, two surfaces consisting of a target shape are considered. It is assumed that the surfaces are topologi-

cally equivalent. The Laplace equation is considered in the domain surrounded by the two surfaces, where Dirichlet boundary conditions with different constant values are imposed. The thickness between these surfaces is defined as the length along with the normal direction of the isosurface of the potential field. Based on this approach, Yezzi et al. [24, 25] proposed the Eulerian approach to directly compute the thickness along with the normal direction. The hybrid Eulerian-Lagrangian approaches were also proposed [26, 27]. The multiple Laplace equation was used for time dependent estimation problems [28]. The main advantage of the PDE approaches is that thickness is uniquely defined at any point. However, the basic idea is restricted under the topological constraint. Furthermore, the inner and outer subsurfaces must be distinguished.

I remark that the proposed method is similar to the Laplacian-based approach. However, the idea is applicable to voxel-based and surface-based data because the proposed PDE can be easily solved using the boundary element method. In addition, the proposed method essentially overcomes the topological problems and does not require dividing surfaces into an inner and outer surface. Furthermore, the proposed PDE is well-posed. That is, the solution is unique and is numerically stable.

Skeleton: The applications of skeleton [29, 30] are found in a broad range of areas, such as medical science, animation, and reverse engineering. As discussed in [31], these methods are categorized to topological thinning methods [15, 32], methods using a distance field [14, 33], geometric methods [34], and methods using the generalized potential field model [35]. The proposed method is closest to the generalized potential field model [36, 37]. The generalized potential field model requires considering a fictitious electrostatic potential field with sources on the surface. The main advantage of the method is that the method provides relatively good results. However, high computational cost is incurred because the Newton potential field is computed by superposition at each point. In addition, these algorithms do not consider numerical stability from a mathematical perspective. Several approaches are proposed to overcome problems related to connectivity and robustness in recent years. For instance,

the erosion thickness approach provides a robust, connected skeleton [38].

Aslan et al. [39] proposed a disconnected skeleton based on the distance function with the heat diffusion equation under a non-zero Dirichlet boundary condition. Aubert et al. [40] used a heat diffusion equation with a constant heat source to extract the distance function and skeleton. Gao et al. [41] presented connected skeleton extraction based on the heat diffusion equation. These heat equation-based methods require precise extraction of ridge curves and calculation of heat diffusion from boundaries within a short time because the Dirichlet boundary condition is imposed at the shape boundaries.

In addition, the PDE-based approaches are used in many related fields as follows:

Image Processing: An elliptic PDE is also extensively used in the image processing. Poisson image editing [42] is a method for image editing that requires solving the Poisson equation. The process requires preserving the gradient of a source image for seamless image editing. Pixels with high gradient are extracted by using the Poisson equation. Poisson matching [43] also uses the Poisson equation in image matching. This basic concept is related to extraction of geometric shape features.

Topology optimization: The use of PDE-based feature evaluation is proposed in topology optimization [44]. The manufacturability in molding is evaluated by superposition of the solution to the PDE. The main advantages of this optimization procedure are the shape and topological sensitivities derived by using the adjoint variable method without restriction in the design space.

3. Concept and Overview

The basic concept of shape features extraction via the use of a steady state partial differential equation (PDE) is geometric shape feature extraction of target geometric features, such as thickness, skeleton, orientation, and curvature, from the target image as a function of the solution to the PDE system, as shown in Figure 1. This paper presents a formulation of a steady state PDE system

Figure 1: Overview of the proposed method: the proposed method extracts geometric shape features, such as thickness, orientation, and skeleton using the solutions of the proposed linear partial differential equation, whose coefficients are given by image data. The left image shows input image data that is used to determine the coefficients. The middle images are solutions to the linear partial differential equation. The three images on the right show various solutions.

and functions for basic geometric features represented by a solution to the PDE system.

The proposed method has the following advantages:

1. Multiple geometric features are computed simultaneously by solving the steady state PDE system.
2. Relatively small shape fractionation on the surface is automatically neglected in the diffusion effect. That is, the method automatically inherits the numerical advantages of the method used to solve the PDE.
3. Thickness extraction does not require any topological constraint and distinction of inner and outer surfaces.
4. The formulation of the PDE and geometric shape feature functions are not dependent on dimension. Any condition on the shape boundaries is not imposed from a numerical perspective.

4. Formulation

4.1. Partial differential equation for geometric shape features extraction

First of all, the steady state linear PDE system is defined for extracting geometric shape features in a binary image. A reference domain Ω_R is considered

that consists of a black domain Ω and a white domain $\Omega_R \setminus \Omega$ whose digital signals are 1 in the black domain and 0 in the white domain. It is assumed that the reference domain Ω_R contains the target image, as shown in Figure 2. Here,

Figure 2: Definitions for formulation

extracting shape features from the black domain Ω is considered. I remark that the shape of the feature in the white domain can be considered in the situation with the opposite signal. Here, I focus on the similarity of shape features when optimizing periodic homogenization [45]. The PDE system is formulated as follows:

$$\begin{cases} -\operatorname{div}(\tilde{a}\nabla s_i - e_i\chi) + \alpha(1 - \chi)s_i = 0 & \text{in } \Omega_R \\ s_i = 0 & \text{on } \partial\Omega_R \end{cases} \quad (1)$$

where $s_i \in H^1(\Omega_R)$ is the i -th state variable, e_i is the canonical base of \mathbb{R}^d , $\tilde{a} \in \mathbb{R}_+$ is the diffusion coefficient, $\alpha \in \mathbb{R}_+$ is the damping coefficient, and d is the dimension. The coefficient α is set to a relatively large value in order to decrease the mutual effect via white domain. The characteristic function $\chi \in L^\infty(\Omega_R)$ is defined as

$$\chi(\mathbf{x}) := \begin{cases} 1 & \text{for } \mathbf{x} \in \Omega \\ 0 & \text{for } \mathbf{x} \in \Omega_R \setminus \Omega. \end{cases} \quad (2)$$

The characteristic function is equivalent to using binary data in the target image. I remark that inside and outside surfaces do not have to be distinguished because domains are distinguished by the characteristic function only in the

same manner as the topology optimization method [46]. In addition, the proposed PDE does not require any topological restriction.

Next, a parameter a is introduced in order for the diffusion coefficient to be satisfied as $\tilde{a} := ah_0^2$, where $h_0 > 0$ is the characteristic length of the target shape size. I remark that the concept of characteristic length is the same as in mechanics. That is, the non-dimensional equation and feature functions defined below are generally reasonable. The damping coefficient α is defined as follows:

$$\alpha := \frac{4}{a} \quad (3)$$

Then, the parameter in the proposed PDE is the non-dimensional diffusion parameter a . The parameter a should be set sufficiently small because the damping coefficient α is defined to prevent effects from the surrounding domain and boundary of the reference domain $\partial\Omega$. That is, the damping coefficient must be set to a large value in order to force the state variables s_i to zero nearly everywhere in the white domain. The number of potential fields defines the dimension, i.e., feature extraction is required for a vector field consisting of independent potential fields.

In order to physically interpret the proposed PDE, the weak and strong forms are derived by introducing a vector field $\mathbf{s} = [s_1, s_2, \dots, s_n]^T$. The weak form is derived as follows:

$$\begin{cases} -\operatorname{div}(\tilde{a}\nabla \mathbf{s} - \operatorname{Id}) = 0 & \text{in } \Omega \\ -\operatorname{div}(\tilde{a}\nabla \mathbf{s}) + \alpha \mathbf{s} = 0 & \text{in } \Omega_R \setminus \Omega \\ \mathbf{s} = 0 & \text{on } \partial\Omega_R \end{cases} \quad (4)$$

As shown in Equation (4), the black domain is governed by the diffusion equation as with the steady state linear elastic equation. The source is shown in the black domain and its magnitude is the divergence of the identity matrix. The damping term decreases the mutual effect via the white domain because the Helmholtz equation governs the behavior of the system in the white domain. Therefore,

the state variable vector \mathbf{s} exponentially converges to the zero vector in the white domain. The strong form is derived as follows:

$$\int_{\Omega_R} (\tilde{a} \nabla \mathbf{s} : \nabla \boldsymbol{\xi}) \, d\Omega + \alpha \int_{\Omega_R \setminus \Omega} \mathbf{s} \cdot \boldsymbol{\xi} \, d\Omega = \int_{\partial\Omega} \mathbf{n} \cdot \boldsymbol{\xi} \, d\Gamma \quad (5)$$

where $\boldsymbol{\xi} \in H_0^1(\Omega_R)^d$ is a test function. The left and right sides are bilinear terms and a source term, respectively. Fictitious traction is applied along the normal direction on the surface $\partial\Omega$ with unit magnitude. Therefore, the state variable vector \mathbf{s} lies along the normal direction of the shape because the damping term is relatively large in the left hand side without domain around the surface $\partial\Omega$. I note that fictitious traction is not directly imposed on the surface $\partial\Omega$.

4.2. Shape feature tensor \mathbb{S}^*

The shape feature tensor \mathbb{S}^* is defined as follows:

$$\mathbb{S}_{ij} (\{s\}_{1 \leq i \leq d}) := \frac{1}{2} \left(\frac{\partial s_i}{\partial x_j} + \frac{\partial s_j}{\partial x_i} \right) \quad (6)$$

The key geometric features are defined using the shape feature tensor \mathbb{S} because the tensor includes all directions of the gradient with respect to the vector \mathbf{s} . Note that the definition of the gradient tensor is not unique. For instance, a strain tensor in linear elastic dynamics includes transpose components. The eigenvalues $\lambda_s^{(i)}$ of the shape feature tensor matrix and the normalized eigenvector $\mathbf{x}_s^{(i)}$, where the order of eigenvalues are defined to satisfy $\lambda_s^{(i)} \leq \lambda_s^{(i+1)}$. Additionally, the state variable \tilde{s}_i using the eigenvector is defined as follows:

$$\begin{pmatrix} \tilde{s}_1 \\ \tilde{s}_2 \\ \vdots \\ \tilde{s}_d \end{pmatrix} := (\mathbf{x}_s^1 \quad \mathbf{x}_s^2 \quad \cdots \quad \mathbf{x}_s^d)^T \begin{pmatrix} s_1 \\ s_2 \\ \vdots \\ s_d \end{pmatrix} \quad (7)$$

4.3. Thickness function

The thickness is inversely proportional to the sum of the derivative of the state variables along each direction of the canonical base. That is, the following defined inverse thickness function f_h is inversely proportional to the local

thickness of the target shape:

$$f_h (\{s\}_{1 \leq i \leq d}) := h_0^2 \left(\sum_{i=1}^d \frac{\partial s_i}{\partial x_i} \right) \chi \quad (8)$$

$$= h_0^2 \left(\sum_{i=1}^d \lambda_s^{(i)} \right) \chi \quad (9)$$

The detailed properties of the inverse thickness function f_h are discussed in Section 7. Using the property with respect to thickness, the thickness function h_f is defined as follows:

$$h_f (\{s\}_{1 \leq i \leq d}) := h_0 \left\{ \frac{1}{f_h (\{s\}_{1 \leq i \leq d})} - a \right\} \chi. \quad (10)$$

The value of the thickness function h_f represents local thickness in the black domain Ω .

4.4. Orientation vector function

As discussed in the weak formulation of the PDE, the state variable vector represents the normal direction on the shape. Therefore, the orientation with respect to the normal direction is formulated as follows:

$$\mathbf{n}_f (\{s\}_{1 \leq i \leq d}) := \frac{1}{\sqrt{\sum_{i=1}^d s_i^2}} \begin{pmatrix} s_1 \\ s_2 \\ \vdots \\ s_d \end{pmatrix} \quad (11)$$

The tangential orientation vector \mathbf{t}_f is computed by applying a rotational transformation to the normal orientation vector \mathbf{n}_f .

4.5. Skeleton function

One of the skeleton functions is formulated as follows:

$$f_s (\{s\}_{1 \leq i \leq d}) := \mathcal{P} \left(\frac{\sqrt{\tilde{s}_1^2}}{\lambda_1} \right) \chi. \quad (12)$$

where \mathcal{P} is a pulse function defined as:

$$\mathcal{P}(x) = \begin{cases} 0 & \text{if } -w > x \\ 1 & \text{if } -w \leq x \leq w \\ 0 & \text{if } w < x \end{cases} \quad (13)$$

The parameter $w > 0$ for width in the non-zero domain should be defined in order to obtain the expected width, e.g., pixel size. The function estimates the medial surfaces in three-dimensions. Therefore, another function may be defined based on the requirements in each application. Note that the function describes a disconnected skeleton [39], and this heuristic formulation is required precise discussions.

5. Numerical Implementation

The computational procedure is essentially the same as the finite element method as follows:

1. The reference domain within the target shape is defined. In general, the reference domain surrounds the input image data.
2. The reference domain is composed of discretized finite elements whose material properties are defined based on the characteristic function χ , which is defined in the input image data.
3. The PDE system (1) is solved using the finite element method. That is, the numerical solution of the state variables $s_i(\mathbf{x})$ are given.
4. The target geometric shape feature is computed from the state variables $s_i(\mathbf{x})$.

This procedure can be easily implemented by using finite element analysis software. The numerical examples shown in Sections 7 and 8 are solved using COMSOL Multiphysics. The boundary element method is also useful for analyzing the proposed PDE if the input data format is surface data, such as STL data.

6. Analytical validation in one dimension

The analytical solutions of the proposed PDE are easily derived in one dimension. A one-dimensional case is considered to validate the proposed method. The distribution of the black domain shown in Figure 3 is considered. The black

Figure 3: An isolated domain in one-dimension

domain exists between $x = p$ and $x = p + h$. The boundary condition is imposed at $x = K$ and $x = L$. These positions are sufficient far from the black domain Ω . The governing equation and boundary condition are

$$(\tilde{a}s')' + \alpha s = 0 \quad \text{if } K \leq x < p \quad (14)$$

$$(\tilde{a}s' - 1)' = 0 \quad \text{if } p \leq x \leq p + h \quad (15)$$

$$(\tilde{a}s')' + \alpha s = 0 \quad \text{if } p + h < x \leq L \quad (16)$$

$$s = 0 \quad \text{on } x = K \quad (17)$$

$$s = 0 \quad \text{on } x = L \quad (18)$$

The analytical solution is derived as follows:

$$s(x) = \begin{cases} c_1 e^{\lambda x} + c_2 e^{-\lambda x} & \text{if } K \leq x < p \\ c_3 x + c_4 & \text{if } p \leq x \leq p + h \\ c_5 e^{\lambda x} + c_6 e^{-\lambda x} & \text{if } p + h < x \leq L \end{cases} \quad (19)$$

where λ is $\lambda = \sqrt{\alpha/\tilde{a}}$. In addition, the thickness function $h_f(s)$ is as follows:

$$h_f(s) = \left(\frac{1}{h_0} \frac{1}{c_3} - h_0 a \right) \mathbf{1}_\Omega \quad (20)$$

The constants c_i are determined based on the boundary conditions (17) and (18), as well as the continuous conditions with respect to the state variable s and normal flux at $x = p$ and $x = p + h$:

$$c_1 = -\frac{h}{\tilde{a}} \left(\frac{e^{\lambda(2L+p)} - e^{\lambda(3p+2h)}}{(2+\lambda h)e^{2\lambda(L+p)} + (\lambda h e^{2\lambda L} + (2-\lambda h)e^{2\lambda(p+h)})e^{2\lambda K} + \lambda h e^{2\lambda(2p+h)}} \right)$$

$$\begin{aligned}
c_2 &= \frac{he^{2\lambda K}}{\tilde{a}} \left(\frac{e^{\lambda(2L+p)} + e^{\lambda(3p+2h)}}{(2+\lambda h)e^{2\lambda(L+p)} + (\lambda h e^{2\lambda L} + (2-\lambda h)e^{2\lambda(p+h)})e^{2\lambda K} + \lambda h e^{2\lambda(2p+h)}} \right) \\
c_3 &= -\frac{2}{\tilde{a}} \left(\frac{e^{2\lambda(K+p+h)} - e^{2\lambda(L+p)}}{(2+\lambda h)e^{2\lambda(L+p)} + (\lambda h e^{2\lambda L} + (2-\lambda h)e^{2\lambda(p+h)})e^{2\lambda K} + \lambda h e^{2\lambda(2p+h)}} \right) \\
c_4 &= \frac{1}{\tilde{a}} \left(\frac{-(2p+h)e^{2\lambda(L+p)} + (he^{2\lambda L} + (2p+h)e^{2\lambda(p+h)})e^{2\lambda K} - he^{2\lambda(2p+h)}}{(2+\lambda h)e^{2\lambda(L+p)} + (\lambda h e^{2\lambda L} + (2-\lambda h)e^{2\lambda(p+h)})e^{2\lambda K} + \lambda h e^{2\lambda(2p+h)}} \right) \\
c_5 &= -\frac{h}{\tilde{a}} \left(\frac{e^{\lambda(2K+p+h)} + e^{\lambda(2p+h)}}{(2+\lambda h)e^{2\lambda(L+p)} + (\lambda h e^{2\lambda L} + (2-\lambda h)e^{2\lambda(p+h)})e^{2\lambda K} + \lambda h e^{2\lambda(2p+h)}} \right) \\
c_6 &= \frac{h}{\tilde{a}} \left(\frac{e^{\lambda(2L+2K+p+h)} + e^{\lambda(2L+3p+h)}}{(2+\lambda h)e^{2\lambda(L+p)} + (\lambda h e^{2\lambda L} + (2-\lambda h)e^{2\lambda(p+h)})e^{2\lambda K} + \lambda h e^{2\lambda(2p+h)}} \right)
\end{aligned}$$

If the black domain is sufficiently far from the boundaries $x = K$ and $x = L$, then the coefficients are simplified as follows:

$$\begin{aligned}
\lim_{\substack{K \rightarrow -\infty \\ L \rightarrow \infty}} c_1 &= -\frac{he^{-\lambda p}}{\tilde{a}(\lambda h + 2)} & \lim_{\substack{K \rightarrow -\infty \\ L \rightarrow \infty}} c_2 &= 0 & \lim_{\substack{K \rightarrow -\infty \\ L \rightarrow \infty}} c_3 &= \frac{2}{\tilde{a}(\lambda h + 2)} \\
\lim_{\substack{K \rightarrow -\infty \\ L \rightarrow \infty}} c_4 &= -\frac{2p+h}{\tilde{a}(\lambda h + 2)} & \lim_{\substack{K \rightarrow -\infty \\ L \rightarrow \infty}} c_5 &= 0 & \lim_{\substack{K \rightarrow -\infty \\ L \rightarrow \infty}} c_6 &= \frac{he^{\lambda(p+h)}}{\tilde{a}(\lambda h + 2)}
\end{aligned}$$

Therefore, the state variable s is simplified as follows:

$$\lim_{\substack{K \rightarrow -\infty \\ L \rightarrow \infty}} s(x) = \begin{cases} \frac{h}{\tilde{a}(\lambda h + 2)} e^{\lambda(x-p)} & \text{if } x < p \\ \frac{1}{\tilde{a}(\lambda h + 2)} (2x - (2p+h)) & \text{if } p \leq x \leq p+h \\ \frac{h}{\tilde{a}(\lambda h + 2)} e^{-\lambda(x-(p+h))} & \text{if } p+h < x. \end{cases} \quad (21)$$

Note that the role of the black domain is to describe damping of the state variable. Therefore, the order of sufficient distance from the black domain is $\frac{1}{\lambda}$, which represents the sharp area of the function $e^{-\lambda x}$.

Finally, the thickness function is derived as follows:

$$\lim_{\substack{K \rightarrow -\infty \\ L \rightarrow \infty}} h_f(s) = \begin{cases} 0 & \text{if } x < p \\ h & \text{if } p \leq x \leq p+h \\ 0 & \text{if } p+h < x \end{cases}. \quad (22)$$

The value of the thickness function in the black domain is exactly equivalent to its thickness h , as long as the black domain is sufficiently far from the boundaries of the reference domain. Therefore, the damping coefficient is set to a relatively

large value in order to satisfy the condition. If the black domain is relatively far from another black domain, the thickness function in the black domain is also exactly equivalent to its thickness h . This case is also confirmed by considering the periodic domain and by taking the limit with respect to the period. Here, the most notable point is that the thickness is extracted without calculating a distance.

The orientation function is obviously well defined because one-dimensional orientation is a sign of the state variable s . The skeleton is defined along one dimension without a base transformation. Then, the skeleton obviously indicates a point at the center of the black domain because the distribution of the state variable $s(x)$ described in Equation (21) is zero at $x = p + \frac{h}{2}$.

The analytical solution of the one-dimensional case can now be presented. Cases (a), (b), and (c) show the effects on h , p , and a , respectively. These parameters are shown in Table 1. As shown in Figure 4, the solution s is

Table 1: Parameters in 1-dimensional calculations

	K	L	h_0	h	p	a
case 1	0.0	1.0	0.2	—	0.2	0.2
case 2	0.0	1.0	0.2	0.2	—	0.2
case 3	0.0	1.0	0.2	0.2	0.4	—

exponentially damped in the white domain and is a linear function in the black domain Ω . The profile of the state variable s is fixed when the parameter p changes as shown in Figure 4(b). Therefore, a shape is equivalently evaluated to the shape whose position has changed. In addition, the effect from another shape or boundary is neglected when the damping coefficient is set to a relatively large value. This arises because the distribution of the state variable s converges exponentially to zero in the white domain, as shown in Figure 4(c). Therefore, it is confirmed that the proposed method can be used to correctly evaluate the geometric features in one dimension.

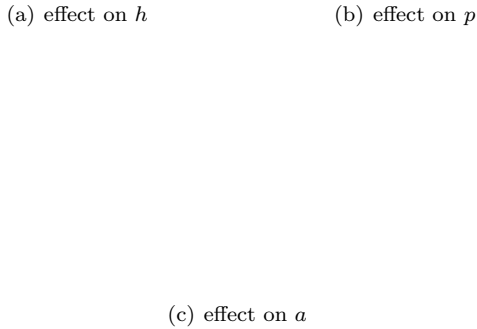


Figure 4: Analytical solutions of the one-dimensional case

I remark that the characteristic length h_0 should be set to approximately the smallest target thickness, because the proposed method is not satisfied in a relatively small shape due to the diffusive nature of the PDE. In other words, relatively small shape fractionation is neglected because the diffusion term requires averaging local information in the PDE system. Although a smaller diffusion coefficient provides more precise evaluation, a small diffusion coefficient is required for a fine finite element mesh in numerical computation. Therefore, the value of a must satisfy the aforementioned situation. In addition, the finite element mesh size is determined by the value of parameter a .

7. Numerical validation in two dimensions

7.1. Multiple bars

The two-dimensional case shown in Figure 5 (a) is considered here. As shown in the figure, the input image data includes multiple bars with thicknesses h of

0.2, 0.25, 0.3, 0.35, 0.4, 0.45, 0.55 and 0.6. The image size is 5×8 . The parameters of the PDE are set to $h_0 = 0.3$ and $a = 0.2$.

The domain is discretized using P2 triangular finite elements with maximum length of 0.05 are used. The obtained state variables s_1 and s_2 are shown in Figures 5 (d) and (e). The normal orientation vector $\mathbf{n}_f(s_1, s_2)$, tangential orientation vector $\mathbf{t}_f(s_1, s_2)$, inverse thickness function $f_h(s_1, s_2)$, thickness function $h_f(s_1, s_2)$, and skeleton function $f_s(s_1, s_2)$ are as shown in Figure 5.

The properties of the inverse thickness function f_h are discussed first. As shown in Figure 5(g), the values are constant in the black domain, excluding near the corners. The relationship between each value of the inverse thickness function f_h and thickness of the bar is plotted in Figure 5(h), where the longitude and abscissa axes are the average value of $1/f_h$ and thickness of the bars, respectively. The average values are computed in each central domain where the width is 5 in order to avoid the corner effect. The linear function estimated with the least squares method is shown in Figure 5(h). The coefficient of determination is $R^2 = 1.0000$. This confirms that the inverse thickness function f_h is inversely proportional to each thickness value. Figure 5(i) also shows the relationship between the value of the thickness function h_f and the thickness of each bar. The blue line shows the linear function estimated with the least squares method. The coefficient of determination in the estimation is also $R^2 = 1.0000$. These results confirm that the thickness function f_h is proportional to each thickness value.

I remark that the linear function does not cross the origin. Although the local thickness is precisely estimated near h_0 , the relatively small thickness is excessively estimated. The effect comes from the diffusion term in the PDE. Therefore, I remark again that the value of h_0 should be set to the smallest thickness.

The value of the thickness function h_f is equivalent to each thickness value, as shown in Figure 5(f). The skeleton shown in Figure 5(c) is also appropriately estimated because the curve is close to the definition of a medial axis [47]. The orientation vectors also provide good estimation, as shown in Figure 5(b).

7.2. Complex shape composed of basic shapes

The effectiveness of the proposed method in with shapes is examined. The image size is set to 1×1 . The parameters of the PDE are set to $h_0 = 0.3$ and $a = 0.2$. The domain is discretized using $\mathbb{P}2$ triangular finite elements.

An image with characteristic shapes is initially considered, as shown in Figure 6. Ring shapes with constant thicknesses located in the bottom portion in the images are considered here. Therefore, the inverse thickness and thickness function values must be constant in each ring shape. It is confirmed that this requirement is satisfied and the expected magnitude of the thickness function h_f is also satisfied. In addition, the orientation vector and skeleton function also indicate appropriate features.

Cubic shapes located in the upper left corner are also considered here. Although each location and angle is different, the thickness function values are equivalent. Thus, it is confirmed that the dependency of these locations and angles are extremely low in the proposed method. In addition, the orientation vectors and skeleton function indicate appropriate features. It is noted that the medial axes of the cubic shapes are its diagonal lines.

Next, I focus on the cross shape located in the center of the image. The intersection is cut to provide a constant thickness with diagonal directions. It is confirmed that the thickness function value at the intersection is appropriate. That is, the thickness is equivalently evaluated as straight bars.

Finally, the full image is considered. The shape and topology of the image are extremely complex. However, all shape features are appropriately extracted simultaneously. That is, the proposed method does not have any topological constraint.

7.3. General shapes

The effectiveness of the proposed method in general shapes is examined. The image size is set to 1×1 in all examples. The parameters of the PDE are set to $h_0 = 0.3$ and $a = 0.2$ in all of the following examples. The reference domain is discretized using $\mathbb{P}2$ triangular finite elements. Three general two

dimensional shapes are considered here, as shown in Figures 7, 8, and 9. As shown, the input images have complex geometric features. The inverse thickness and thickness function values are globally appropriate, as shown in these figures. In the local perspective, sharply dented shapes are estimated as a thick shape. In addition, a relatively small fluctuated shape is neglected because the small feature is averaged by the diffusion effect in the PDE. The orientation vectors and skeleton are also globally appropriate. However, unconnected skeletons are obtained, because the proposed function is defined based on the concept of the medial axis and does not consider connectivity. Therefore, different functions must be considered.

7.4. Tari's Dataset

All shapes in Tari's dataset [48] are considered in order to provide a comparison with related research. The dataset includes noisy images and that are used as a benchmark shapes in skeleton extraction [41, 49, 50, 39]. The image size is set to 2×1.5 in Figure 10. The parameters of the PDE are set to $h_0 = 0.05$ and $a = 0.2$. The reference domain is discretized using $\mathbb{P}2$ triangular finite elements. The obtained results are consistent with results from the literature [41, 49, 50, 39]. However, the obtained skeleton is disconnected. Therefore, the proposed skeleton extraction results are similar to Aslan's results [39].

8. Numerical validation in three dimensions

8.1. Multiple boxes

The proposed method is used with three-dimensional cases in this section. A simple three-dimensional case shown in Figure 11 (a) is initially considered. The box sizes are $0.7 \times 0.9 \times 0.1$, $0.7 \times 0.9 \times 0.15$, and $0.7 \times 0.9 \times 0.2$. Therefore, each thickness is 0.1, 0.15, and 0.2, excluding the thickness near the edges. The parameters of PDE are set to $h_0 = 0.1$ and $a = 0.2$. The domain is discretized using $\mathbb{P}2$ tetrahedral finite elements.

As shown, the thickness function values are appropriate and the thickness function h_f is effective in three dimensions. The obtained orientation vectors are

also appropriate, because the orientation is equivalent to the normal direction of each surface. The orientation vector on the cross-sectional surface shown in Figure 11(c) is equivalent to the rectangular case in two dimensions. In addition, it is confirmed that the skeleton function is equivalent to the medial surface. Therefore, the proposed method can be used in simple three-dimensional cases.

8.2. Complex and general shapes

The effectiveness of the proposed method with general three-dimensional shapes is examined. The parameters of the PDE are set to $h_0 = 0.1$ and $a = 0.2$ in all of the following examples. The domain is discretized using P2 tetrahedral finite elements.

Figures 12, 13, and 14 show numerical examples for topologically complex shapes. In particular, Figure 14 shows a double Möbius band model. That is, the surfaces cannot be divided into inner and outer surfaces. As shown, the proposed method appropriately provides these geometric features without any topological constraint. In addition, the local thickness is computed without distinction between inner and outer surfaces.

Figures 15 and 16 show shapes with relatively small fluctuations. As shown, these cases are also appropriately computed for these geometrical features.

9. Conclusions and future work

This paper presents a unified method for extracting geometric shape features using a steady state PDE. The following results and conclusions were reached:

1. A steady state PDE was formulated for extracting geometric features.
2. The functions for orientation vector, inverse thickness, thickness, and skeleton were formulated as the solutions to the proposed PDE.
3. The analytical solution was derived in the one-dimensional case. The derived solution demonstrates the validity of the proposed function.
4. Several numerical examples were presented to confirm the usefulness of the proposed method for the various geometric shape features examined

in this paper. In addition, it was confirmed that these geometric shape features were extracted without requiring any topological constraint.

Functions for other geometric features, such as curved skeleton, will be considered mathematically in the future. In particular, heuristic formulations with respect to the thickness and the skeleton are required to obtain more precise extraction. The formulation will also be extended to gray images in order to expand the range of applications.

Acknowledgment

The author acknowledges comments from Professor Grégoire Allaire (École Polytechnique) regarding validation of the proposed model. This work was supported in part by research grants from The Kyoto Technoscience Center and JSPS KAKENHI Grant Number 16K05039.

References

- [1] N. Yamashita, S. Yoshizawa, H. Yokota, Volume-based shape analysis for internal microstructure of steels, in: 2014 IEEE International Conference on Image Processing, IEEE, 2014, pp. 4887–4891. [doi:10.1109/ICIP.2014.7025990](https://doi.org/10.1109/ICIP.2014.7025990).
- [2] P. Benko, R. R. Martin, T. Varady, Algorithms for reverse engineering boundary representation models, Computer-Aided Design 33 (11) (2001) 839–851. [doi:doi.org/10.1016/S0010-4485\(01\)00100-2](https://doi.org/10.1016/S0010-4485(01)00100-2).
- [3] T. Sera, H. Fujioka, H. Yokota, A. Makinouchi, R. Himeno, R. C. Schroter, K. Tanishita, Three-dimensional visualization and morphometry of small airways from microfocal X-ray computed tomography, Journal of biomechanics 36 (11) (2003) 1587–1594. [doi:10.1016/S0021-9290\(03\)00179-9](https://doi.org/10.1016/S0021-9290(03)00179-9).
- [4] M. Zhenjiang, Zernike moment-based image shape analysis and its application, Pattern Recognition Letters 21 (2) (2000) 169–177. [doi:10.1016/S0167-8655\(99\)00144-0](https://doi.org/10.1016/S0167-8655(99)00144-0).

- [5] T. Hildebrand, P. Rüegsegger, A new method for the model-independent assessment of thickness in three-dimensional images, *Journal of Microscopy* 185 (1) (1997) 67–75. [doi:10.1046/j.1365-2818.1997.1340694.x](https://doi.org/10.1046/j.1365-2818.1997.1340694.x).
- [6] C. Hutton, E. De Vita, J. Ashburner, R. Deichmann, R. Turner, Voxel-based cortical thickness measurements in MRI, *Neuroimage* 40 (4) (2008) 1701–1710. [doi:10.1016/j.neuroimage.2008.01.027](https://doi.org/10.1016/j.neuroimage.2008.01.027).
- [7] T. Fujimori, H. Suzuki, Surface extraction from multi-material CT data, in: Ninth International Conference on Computer Aided Design and Computer Graphics, IEEE, 2005, p. 6. [doi:10.1109/CAD-CG.2005.79](https://doi.org/10.1109/CAD-CG.2005.79).
- [8] P. K. Saha, Tensor scale: A local morphometric parameter with applications to computer vision and image processing, *Computer Vision and Image Understanding* 99 (3) (2005) 384–413. [doi:10.1016/j.cviu.2005.03.003](https://doi.org/10.1016/j.cviu.2005.03.003).
- [9] F. A. Andaló, P. A. Miranda, R. d. S. Torres, A. X. Falcão, Shape feature extraction and description based on tensor scale, *Pattern Recognition* 43 (1) (2010) 26–36. [doi:10.1016/j.patcog.2009.06.012](https://doi.org/10.1016/j.patcog.2009.06.012).
- [10] K. Crane, C. Weischedel, M. Wardetzky, Geodesics in heat: A new approach to computing distance based on heat flow, *ACM Transactions on Graphics* 32 (5) (2013) 152. [doi:10.1145/2516971.2516977](https://doi.org/10.1145/2516971.2516977).
- [11] P. K. Saha, F. W. Wehrli, Measurement of trabecular bone thickness in the limited resolution regime of in vivo MRI by fuzzy distance transform, *IEEE Transactions on Medical Imaging* 23 (1) (2004) 53–62. [doi:10.1109/TMI.2003.819925](https://doi.org/10.1109/TMI.2003.819925).
- [12] Y. Liu, D. Jin, C. Li, K. F. Janz, T. L. Burns, J. C. Torner, S. M. Levy, P. K. Saha, A robust algorithm for thickness computation at low resolution and its application to in vivo trabecular bone CT imaging, *IEEE Transactions on Biomedical Engineering* 61 (7) (2014) 2057–2069. [doi:10.1109/TBME.2014.2313564](https://doi.org/10.1109/TBME.2014.2313564).

- [13] P. K. Saha, F. W. Wehrli, B. R. Gomberg, Fuzzy distance transform: Theory, algorithms, and applications, *Computer Vision and Image Understanding* 86 (3) (2002) 171–190. [doi:10.1006/cviu.2002.0974](https://doi.org/10.1006/cviu.2002.0974).
- [14] C. Arcelli, G. S. di Baja, L. Serino, Distance-driven skeletonization in voxel images, *IEEE Transactions on Pattern Analysis and Machine Intelligence* 33 (4) (2011) 709–720. [doi:10.1109/TPAMI.2010.140](https://doi.org/10.1109/TPAMI.2010.140).
- [15] P. K. Saha, B. B. Chaudhuri, D. D. Majumder, A new shape preserving parallel thinning algorithm for 3D digital images, *Pattern Recognition* 30 (12) (1997) 1939–1955. [doi:10.1016/S0031-3203\(97\)00016-2](https://doi.org/10.1016/S0031-3203(97)00016-2).
- [16] M. J. Clarkson, M. J. Cardoso, G. R. Ridgway, M. Modat, K. K. Leung, J. D. Rohrer, N. C. Fox, S. Ourselin, A comparison of voxel and surface based cortical thickness estimation methods, *Neuroimage* 57 (3) (2011) 856–865. [doi:10.1016/j.neuroimage.2011.05.053](https://doi.org/10.1016/j.neuroimage.2011.05.053).
- [17] C. Davatzikos, N. Bryan, Using a deformable surface model to obtain a shape representation of the cortex, *IEEE Transactions on Medical Imaging* 15 (6) (1996) 785–795. [doi:10.1109/42.544496](https://doi.org/10.1109/42.544496).
- [18] X. Han, D. L. Pham, D. Tosun, M. E. Rettmann, C. Xu, J. L. Prince, CRUISE: Cortical reconstruction using implicit surface evolution, *NeuroImage* 23 (3) (2004) 997–1012. [doi:10.1016/j.neuroimage.2004.06.043](https://doi.org/10.1016/j.neuroimage.2004.06.043).
- [19] G. Lohmann, C. Preul, M. Hund-Georgiadis, Morphology-based cortical thickness estimation, in: *Biennial International Conference on Information Processing in Medical Imaging*, Springer, 2003, pp. 89–100. [doi:10.1007/978-3-540-45087-0_8](https://doi.org/10.1007/978-3-540-45087-0_8).
- [20] I. Aganj, G. Sapiro, N. Parikshak, S. K. Madsen, P. M. Thompson, Measurement of cortical thickness from MRI by minimum line integrals on soft-classified tissue, *Human Brain Mapping* 30 (10) (2009) 3188–3199. [doi:10.1002/hbm.20740](https://doi.org/10.1002/hbm.20740).

- [21] M. L. Scott, P. A. Bromiley, N. A. Thacker, C. Hutchinson, A. Jackson, A fast, model-independent method for cerebral cortical thickness estimation using MRI, *Medical Image Analysis* 13 (2) (2009) 269–285. [doi:10.1016/j.media.2008.10.006](https://doi.org/10.1016/j.media.2008.10.006).
- [22] S. R. Das, B. B. Avants, M. Grossman, J. C. Gee, Registration based cortical thickness measurement, *Neuroimage* 45 (3) (2009) 867–879. [doi:10.1016/j.neuroimage.2008.12.016](https://doi.org/10.1016/j.neuroimage.2008.12.016).
- [23] S. E. Jones, B. R. Buchbinder, I. Aharon, Three-dimensional mapping of cortical thickness using Laplace’s equation, *Human Brain Mapping* 11 (1) (2000) 12–32.
- [24] A. J. Yezzi, J. L. Prince, An eulerian pde approach for computing tissue thickness, *IEEE Transactions on Medical Imaging* 22 (10) (2003) 1332–1339. [doi:10.1109/TMI.2003.817775](https://doi.org/10.1109/TMI.2003.817775).
- [25] A. Yezzi, J. L. Prince, A PDE approach for measuring tissue thickness, in: *Proceedings of the 2001 IEEE Computer Society Conference on Computer Vision and Pattern Recognition*, Vol. 1, IEEE, 2001, pp. I–I. [doi:10.1109/CVPR.2001.990460](https://doi.org/10.1109/CVPR.2001.990460).
- [26] K. R. Rocha, A. J. Yezzi, J. L. Prince, A hybrid Eulerian-Lagrangian approach for thickness, correspondence, and gridding of annular tissues, in: *International Workshop on Computer Vision for Biomedical Image Applications*, Springer, 2005, pp. 72–81.
- [27] O. Acosta, P. Bourgeat, M. A. Zuluaga, J. Fripp, O. Salvado, S. Ourselin, Automated voxel-based 3D cortical thickness measurement in a combined Lagrangian–Eulerian PDE approach using partial volume maps, *Medical Image Analysis* 13 (5) (2009) 730–743. [doi:10.1016/j.media.2009.07.003](https://doi.org/10.1016/j.media.2009.07.003).
- [28] M. J. Cardoso, M. J. Clarkson, M. Modat, S. Ourselin, On the extraction of topologically correct thickness measurements using Khalim-

skys cubic complex, in: Biennial International Conference on Information Processing in Medical Imaging, Springer, 2011, pp. 159–170. doi: [10.1007/978-3-642-22092-0_14](https://doi.org/10.1007/978-3-642-22092-0_14).

- [29] U. Montanari, A method for obtaining skeletons using a quasi-Euclidean distance, *Journal of the ACM* 15 (4) (1968) 600–624. doi: [10.1145/321479.321486](https://doi.org/10.1145/321479.321486).
- [30] H. Blum, R. N. Nagel, Shape description using weighted symmetric axis features, *Pattern Recognition* 10 (3) (1978) 167–180. doi: [10.1016/0031-3203\(78\)90025-0](https://doi.org/10.1016/0031-3203(78)90025-0).
- [31] N. D. Cornea, D. Silver, P. Min, Curve-skeleton properties, applications, and algorithms, *IEEE Transactions on Visualization And Computer Graphics* 13 (3) (2007) 0530–548. doi: [10.1109/TVCG.2007.1002](https://doi.org/10.1109/TVCG.2007.1002).
- [32] K. Palágyi, A. Kuba, A 3D 6-subiteration thinning algorithm for extracting medial lines, *Pattern Recognition Letters* 19 (7) (1998) 613–627. doi: [10.1016/S0167-8655\(98\)00031-2](https://doi.org/10.1016/S0167-8655(98)00031-2).
- [33] I. Bitter, A. E. Kaufman, M. Sato, Penalized-distance volumetric skeleton algorithm, *IEEE Transactions on Visualization and Computer Graphics* 7 (3) (2001) 195–206. doi: [10.1109/2945.942688](https://doi.org/10.1109/2945.942688).
- [34] N. Amenta, S. Choi, R. K. Kolluri, The power crust, unions of balls, and the medial axis transform, *Computational Geometry* 19 (2-3) (2001) 127–153. doi: [10.1016/S0925-7721\(01\)00017-7](https://doi.org/10.1016/S0925-7721(01)00017-7).
- [35] G. H. Abdel-Hamid, Y.-H. Yang, Multiresolution skeletonization an electrostatic field-based approach, in: Proceedings of 1st International Conference on Image Processing, Vol. 1, IEEE, 1994, pp. 949–953. doi: [10.1109/ICIP.1994.413249](https://doi.org/10.1109/ICIP.1994.413249).
- [36] N. Ahuja, J.-H. Chuang, Shape representation using a generalized potential field model, *IEEE Transactions on Pattern Analysis and Machine Intelligence* 19 (2) (1997) 169–176. doi: [10.1109/34.574801](https://doi.org/10.1109/34.574801).

- [37] T. Grigorishin, G. Abdel-Hamid, Y.-H. Yang, Skeletonisation: An electrostatic field-based approach, *Pattern Analysis and Applications* 1 (3) (1998) 163–177. [doi:10.1007/BF01259366](https://doi.org/10.1007/BF01259366).
- [38] Y. Yan, K. Sykes, E. Chambers, D. Letscher, T. Ju, Erosion thickness on medial axes of 3D shapes, *ACM Transactions on Graphics* 35 (4) (2016) 38. [doi:10.1145/2897824.2925938](https://doi.org/10.1145/2897824.2925938).
- [39] C. Aslan, A. Erdem, E. Erdem, S. Tari, Disconnected skeleton: Shape at its absolute scale, *IEEE Trans. Pattern Anal. Mach. Intell.* 30 (12) (2008) 2188–2203. [doi:10.1109/TPAMI.2007.70842](https://doi.org/10.1109/TPAMI.2007.70842).
- [40] G. Aubert, J.-F. Aujol, Poisson skeleton revisited: A new mathematical perspective, *Journal of Mathematical Imaging and Vision* 48 (1) (2014) 149–159. [doi:10.1007/s10851-012-0404-5](https://doi.org/10.1007/s10851-012-0404-5).
- [41] F. Gao, G. Wei, S. Xin, S. Gao, Y. Zhou, 2d skeleton extraction based on heat equation, *Computers & Graphics* 74 (2018) 99–108. [doi:10.1016/j.cag.2018.05.005](https://doi.org/10.1016/j.cag.2018.05.005).
- [42] P. Pérez, M. Gangnet, A. Blake, Poisson image editing, *ACM Transactions on Graphics* 22 (3) (2003) 313–318. [doi:10.1145/1201775.882269](https://doi.org/10.1145/1201775.882269).
- [43] J. Sun, J. Jia, C.-K. Tang, H.-Y. Shum, Poisson matting, in: *ACM Transactions on Graphics*, Vol. 23, 2004, pp. 315–321. [doi:10.1145/1186562.1015721](https://doi.org/10.1145/1186562.1015721).
- [44] Y. Sato, T. Yamada, K. Izui, S. Nishiwaki, Manufacturability evaluation for molded parts using fictitious physical models, and its application in topology optimization, *The International Journal of Advanced Manufacturing Technology* 92 (1-4) (2017) 1391–1409. [doi:10.1007/s00170-017-0218-0](https://doi.org/10.1007/s00170-017-0218-0).
- [45] G. Allaire, T. Yamada, Optimization of dispersive coefficients in the homogenization of the wave equation in periodic structures, *Numerische Mathematik* in press (-) (2018) –. [doi:10.1007/s00211-018-0972-4](https://doi.org/10.1007/s00211-018-0972-4).

- [46] T. Yamada, K. Izui, S. Nishiwaki, A. Takezawa, A topology optimization method based on the level set method incorporating a fictitious interface energy, *Computer Methods in Applied Mechanics and Engineering* 199 (45) (2010) 2876–2891. [doi:10.1016/j.cma.2010.05.013](https://doi.org/10.1016/j.cma.2010.05.013).
- [47] H. Blum, A transformation for extracting new descriptors of shape, *Models for Perception of Speech and Visual Forms* (1967) 362–380.
- [48] C. Asian, S. Tari, An axis-based representation for recognition, in: *Tenth IEEE International Conference on Computer Vision (ICCV'05)* Volume 1, Vol. 2, IEEE, 2005, pp. 1339–1346. [doi:10.1109/ICCV.2005.32](https://doi.org/10.1109/ICCV.2005.32).
- [49] W. Shen, X. Bai, R. Hu, H. Wang, L. J. Latecki, Skeleton growing and pruning with bending potential ratio, *Pattern Recognition* 44 (2) (2011) 196–209. [doi:10.1016/j.patcog.2010.08.021](https://doi.org/10.1016/j.patcog.2010.08.021).
- [50] W. Shen, X. Bai, X. Yang, L. J. Latecki, Skeleton pruning as trade-off between skeleton simplicity and reconstruction error, *Science China Information Sciences* 56 (4) (2013) 1–14. [doi:10.1007/s11432-012-4715-3](https://doi.org/10.1007/s11432-012-4715-3).

(a) Input image data, where the image size is 5×8 . The black and white colors show the black and white domains, respectively.

(b) Orientation vectors, where the blue and red colors indicate the normal and tangential vectors, respectively. The gray and white domain colors are the input image data for reference.

(c) Skeleton function $f_s(s_1, s_2)$. The gray and white domain colors are the input image data for reference.

(d) Distribution of the state variable s_1

(e) Distribution of the state variable s_2

(f) Thickness function $h_f(s_1, s_2)$

(g) Inverse thickness function $f_h(s_1, s_2)$

(h) Plot of the average value of $\frac{1}{f_h}$ in the central domain of each bar and the linear function estimated with the least squares method

(i) Plot of the average value of h_f in the central domain of each bar and the linear function estimated with the least squares method

Figure 5: Numerical results for an image of multiple bars with different thicknesses

(a) Input image data (b) Inverse thickness function $f_h(s_1, s_2)$ (c) Thickness function $h_f(s_1, s_2)$

(d) Orientation vectors (e) Skeleton function $f_s(s_1, s_2)$.

Figure 6: Numerical example of a two-dimensional complex shape

(a) Input image data (b) Inverse thickness function $f_h(s_1, s_2)$ (c) Thickness function $h_f(s_1, s_2)$

(d) Orientation vectors (e) Skeleton function $f_s(s_1, s_2)$.

Figure 7: Case 1 of a general shape in two dimensions

(a) Input image data (b) Inverse thickness function $f_h(s_1, s_2)$ (c) Thickness function $h_f(s_1, s_2)$

(d) Orientation vectors (e) Skeleton function $f_s(s_1, s_2)$.

Figure 8: Case 2 of a general shape in two dimensions

(a) Input image data (b) Inverse thickness function $f_h(s_1, s_2)$ (c) Thickness function $h_f(s_1, s_2)$

(d) Orientation vectors (e) Skeleton function $f_s(s_1, s_2)$.

Figure 9: Case 3 of a general shape in two dimensions

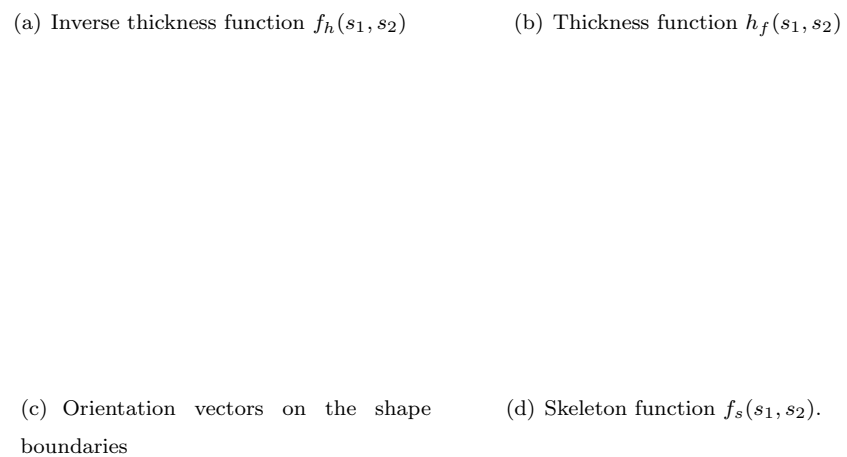


Figure 10: Results with Taris' dataset using the proposed method

(a) Input data

(b) Orientation vectors on the faces

(c) Orientation vectors on the cross-sectional surfaces

(d) Inverse thickness function

(e) Thickness function

$f_h(s_1, s_2, s_3)$ $h_f(s_1, s_2, s_3)$.

(f) Skeleton function $f_s(s_1, s_2, s_3)$ on the cross-sectional surfaces.

Figure 11: Box shapes with different thicknesses

(a) Input data (b) Orientation vectors (c) Inverse thickness
 on the surfaces function $f_h(s_1, s_2, s_3)$

(d) Thickness function (e) Skeleton function
 $h_f(s_1, s_2, s_3)$. $f_s(s_1, s_2, s_3)$ on the
 cross-sectional surfaces.

Figure 12: C-type ring

(a) Input data (b) Orientation vec- (c) Inverse thickness
 tors on the surfaces function $f_h(s_1, s_2, s_3)$

(d) Thickness function (e) Skeleton function
 $h_f(s_1, s_2, s_3)$. $f_s(s_1, s_2, s_3)$ on
 the cross-sectional
 surfaces.

Figure 13: Crossed rings

(a) Input data (b) Orientation vectors (c) Inverse thickness function
 $\mathbf{n}_f(s_1, s_2, s_3)$

(d) Thickness function
 $h_f(s_1, s_2, s_3)$.

(e) Skeleton function
 $f_s(s_1, s_2, s_3)$ on the cross-sectional surfaces.

Figure 14: Double Mobius band model

(a) Input data (b) Orientation vectors (c) Inverse thickness function
 $\mathbf{n}_f(s_1, s_2, s_3)$

(d) Thickness function (e) Skeleton function
 $h_f(s_1, s_2, s_3)$. $f_s(s_1, s_2, s_3)$
 on the cross-sectional surfaces.

Figure 15: Arm model

(a) Input data (b) Orientation vec- (c) Inverse thickness func-
tors $\mathbf{n}_f(s_1, s_2, s_3)$ tion $f_h(s_1, s_2, s_3)$

(d) Thickness function $f_h(s_1, s_2, s_3)$. (e) Skeleton func-
tion $f_s(s_1, s_2, s_3)$ on
the cross-sectional
surfaces.

Figure 16: The Stanford bunny model